WILEY | Hindawi

Research Article

Simulation of the Compression Testing of Additively Manufactured Lattice Structures Using Inputs from Microcomputed Tomography

Minsol Park ,[1] **Martin Philip Venter ,**[1] **and Anton Du Plessis** [2,3]

[1]Department of Mechanical and Mechatronics Engineering, University of Stellenbosch, South Africa
[2]Department of Physics, University of Stellenbosch, South Africa
[3]Object Research Systems Inc, Montreal, Canada

Correspondence should be addressed to Minsol Park; minimum3701@gmail.com

Finite element (FE) modeling is a powerful tool for the virtual testing of components, especially for high-value manufacturing like additive manufacturing (AM). AM often involves lattice structures in parts, imparting unique mechanical properties. Numerical models allow for cost-effective virtual testing, but computational limitations hinder comprehensive investigations on lattice structures, and idealized models may not fully represent actual manufactured behavior. This study proposes a simplified numerical model for analyzing lattice structure compression behavior before failure, incorporating X-ray microcomputed tomography (CT) scan data. The model includes real manufacturing defects, such as geometrical inaccuracies, internal porosity, and surface roughness. It closely fits compression test results from samples with varied defects, with a maximum error of 17% for stiffness, 13% for yield stress, and 7% for peak stress. The model offers promise for developing manufacturing defect-incorporated lattice representative volume elements (RVEs) to design AM parts with lattice regions. Replacing complex lattice structures with solid-infilled RVEs in simulations reduces computational costs significantly. This approach allows efficient exploration of lattice AM components' mechanical behavior, accounting for manufacturing defects and offering insights for design optimization and material selection.

1. Introduction

Laser powder bed fusion (L-PBF) is significantly changing the manufacturing of all kinds of metallic components, allowing new designs with increased complexity to be manufactured compared to traditional manufacturing methods. One highly popular design approach involved the use of intricate cellular architectures, or lattice structures, which offer superior mechanical properties when compared to conventional stochastic foams [1]. This innovation has facilitated the local customization of mechanical properties, enabling the creation of novel metamaterials with unique properties derived from the bulk material [2]. Lattice structures are particularly valuable in high-end engineering fields such as biomedical [3] and aerospace [4], where specific mechanical properties are essential. For example, they can

be employed to match the mechanical properties of a manufactured titanium implant with that of bones in biomedical engineering or achieve high strength-to-weight ratios in aerospace and automotive engineering.

The current utilization of lattice structures is limited to high-end engineering fields due to the high manufacturing cost and concerns over their reliability [5]. Material characterization of lattice structures is essential due to their small feature sizes and sensitivity to process parameters that can lead to reduced quality of the parts. Ideally, this is performed on small-scale test samples before printing large, complex parts to avoid wastage in manufacturing cost and time. The mechanical testing of coupons is a typical experimental approach, which is simple and reliable [6, 7]. Nevertheless, all forms of mechanical testing are relatively costly and time-consuming, since test parts need to be manufactured,

and the availability of suitable experimental setups can be limited. Numerical methods, on the other hand, offer more cost-effective solutions as the manufacturing process or experimental setups do not limit them. The numerical analysis offers the ability to investigate parameters that can be challenging to attain in experiments, such as varying strut size [8], different cell configuration designs [9], and investigating a wider range of manufacturing defects [10] to understand their influence and understand the safety margins for these structures. Examples of simulation studies involving lattice structures include, for instance, Güden et al. [8] who employed a numerical model to study the effect of the number of cells, strut diameter, and face sheet on the compression of BBC lattices. Barnes et al. [9] used numerical simulations to investigate the mechanical behavior of lattice structures with hybrid topologies and the relationship between localized states of stress and the global behavior of hybrid lattice structures.

Qureshi et al. [10] explored the impact of porosity and functional grading on the heat transfer efficiency of triply periodic minimal surface (TPMS) topologies. Weeger et al. [11] examined complex nonlinear and inelastic effects during large deformations through the use of inelastic beam models. Their findings underscore the significance of considering nonlinear and inelastic effects in such analyses.

However, it is important to note that numerical results may not always match experimental results due to discrepancies in as-designed models and as-built samples. The as-designed model has an idealized geometry without manufacturing defects, whereas as-built models contain various manufacturing defects including geometrical inaccuracies [12], internal porosity [7, 13], and surface roughness [14]. These defects are potentially detrimental to mechanical properties. The as-designed numerical model without manufacturing defect consideration normally overestimates the mechanical properties of real manufactured lattice structures.

To account for the impact of manufacturing defects on the FE models, some researchers have adopted micro-CT. This is a nondestructive imaging and analysis tool capable of generating a three-dimensional digital model for inspecting both external and internal geometrical features [15]. X-ray CT is a promising tool for evaluating the geometrical accuracy of AM lattice structures, including measuring the geometrical difference between as-built and as-designed structures and identifying manufacturing defects [16]. It is widely used in various nondestructive analyses, such as surface topography evaluation, porosity analysis, and coordinate measurements. Simulation on micro-CT scan digital models indeed has the potential to minimize the gap between numerical and experimental results, as it allows for a more accurate representation of the real lattice structures with their manufacturing defects [17]. However, the use of CT scan digital models in simulations is constrained by computational time and cost due to the inherent complexity of their geometry, which includes intricate details of irregular surface morphology and internal porosity. To overcome this limitation, researchers have proposed various approaches to develop FE models that can provide accept-

able accuracy with reduced computational time. These approaches are aimed at simplifying the geometry of the FE model while maintaining its accuracy. Such approaches include homogenization techniques [18], RVE techniques [18, 19], and geometry simplification [20, 21].

The RVE is a fraction of the volume representing the entire structure's properties [19]. By employing RVE modeling with periodic boundary conditions, the computational time of FE modeling can be significantly reduced. Homogenization, a technique used to determine the global properties of structures with repetitive features, is commonly incorporated with RVE. This enables the development of a numerical model that accurately represents the lattice structure. Park et al. [18] utilized homogenization in two stages to model lattice structures with geometrical inaccuracies. They divided the scale levels into layer deposition, structural element, and lattice structure, proposing transformations between them to estimate effective properties. The method involves finding geometrical and material properties of structural elements and then estimating effective mechanical properties of lattice material using a unit cell and discretized homogenization for periodic structures. This allowed them to accurately capture the behavior of the lattice structure while significantly reducing the computational cost.

Another commonly used method for reducing computational complexity is simplifying the imperfect geometric features of the strut, such as surface roughness and strut thickness deviation. Cao et al. [20] proposed FE models with simplified geometry features that use probability distribution functions of deviation of strut porosity, strut waviness, and strut radius. The results showed that the statistical model better agrees with the experiment than the ideal model (without defects). Similarly, Lozanovski et al. [21] developed FE models of lattice structures using representative strut FE models that incorporate AM inherent defects. They observed a significantly increased correlation between the representative FE model and the experiment compared to the ideal geometry model. Ghosh et al. [22] presented a tensile loading simulation on microstrut models with sharp notch-like features to demonstrate the effect of surface roughness on mechanical performance. Their findings revealed that the yield strength and ultimate tensile strength (UTS) of the microstrut under tensile loading increase with the size of the notch feature. This is attributed to the notch-strengthening effect caused by the presence of surface notches [23].

Despite numerous approaches to incorporate manufacturing defects into numerical models, the simultaneous integration of geometrical inaccuracies, internal porosity, and surface roughness remains an unexplored area in the existing literature. In response, this study proposes a novel numerical approach for lattice compression tests that addresses this gap by utilizing inputs from CT scans of coupon samples to incorporate manufacturing defects. Instead of importing the entire CT scan to the FE model, the analysis focuses on quantifying the level of manufacturing defects. Subsequently, using information gathered from the CT scan, the corresponding level of defects is incorporated into the FE models. This approach effectively reduces computational requirements compared to direct entire CT scan importing methods, making it a practical

and efficient solution. The present work also conducted work on parametric investigations of different defect types individually, to investigate their relative influence on properties. This level of analysis would not be achievable with compression tests on real printed samples due to the cost and difficulty in inducing specific defect types individually. The proposed model can serve as a RVE that incorporates manufacturing defects in lattice structures. This feature is beneficial for industry users as they can utilize this RVE to develop numerical models that accurately homogenize lattice structures by replacing them with solid-infilled features in simulations for larger end-use parts containing lattice regions. This substitution substantially reduces the computational expense associated with modeling complex lattice structures in such situations. By employing the lattice RVE, users can efficiently study the mechanical behavior of lattice structures with manufacturing defects and gain valuable insights for optimizing their design and performance.

2. Numerical Model Input Data Collection

2.1. Manufacturing and CT Scans. Lattice coupon samples were manufactured to obtain CT scan data for designing manufacturing defect-incorporated FE models. Diamond lattice structures, composed of 10 unit cells along each axis with a density of 20%, were produced using Ti6Al4V powders. The EOS M290 system was utilized, employing the default process parameters for this material, which included a laser power of 280 W, a layer thickness of 30 μm, a scanning speed of 1200 mm/s, and a zigzag formation scanning strategy with a 67-degree rotation.

The lattice coupon samples were manufactured on a Ti6Al4V base plate with dimensions of $250 \times 250 \times 25$ mm, utilizing an argon flowing chamber during fabrication. Following manufacturing, the lattice structures underwent a standard stress-relief heat treatment at 650 degrees Celsius for 3 hours. The samples were then removed from the platform through cutting.

To intentionally induce the manufacturing defects in the lattice structure to make it a flawed condition, the process parameter layer thickness and laser power were varied. Each lattice structure was labeled based on its corresponding process parameter settings, with "P" and "T" representing laser power and layer thickness, respectively. The specific values for each parameter are indicated by subsequent numbers. For instance, P280-T30 refers to a lattice structure produced with a laser power of 280 W and a layer thickness of 30 μm. The process parameters, laser power, and layer thickness were varied from the reference sample, P280-T30, which was produced using the recommended settings for Ti64 ELI for the EOSM290 machine. The layer thickness was adjusted to 60 μm (sample P280-T60) and 90 μm (sample P280-T90), keeping laser power constant to 280 W, while the laser power was varied to 210 W (sample P210-T30) and 360 W (sample P360-T30), keeping layer thickness constant to 30 μm.

The lattice coupons underwent micro-CT scanning using the General Electric Phoenix VTomeX L240 system [24]. The scanning process involved capturing 3000 images

with the assistance of a beam filter. The setup parameters included a voxel size of 25 μm (CT scan resolution), a voltage of 130 kV, and a current of 100 μA. The CT scan analysis was performed in *Dragonfly* software, developed by Object Research Systems, to assess manufacturing defects such as geometric inaccuracies, internal porosity, and surface roughness. Internal porosity is defined as the proportion of the volume occupied by internal voids to the total material volume. Surface roughness, on the other hand, characterizes the irregularities on the surface of lattice structure struts and was assessed using R_a values. Geometric inaccuracies were analyzed using three parameters: cylindrical diameter, strut thickness, and node thickness. These terms were defined in our paper currently under review [25]. Strut thickness specifically refers to the thickness of the individual struts, excluding the nodes where they intersect. Node thickness, conversely, represents the thickness of the regions where the struts are interconnected. The cylindrical diameter represents the size of a cylinder that fully encompasses both the struts and nodes of the lattice structure. It serves as an average measure of the combined thickness of the struts and nodes. The CT scan analysis yielded quantitative data on geometric inaccuracies, internal porosity, and surface roughness, as summarized in Table 1. These data were utilized as inputs for the FE models. However, it is essential to acknowledge that obtaining the internal porosity of sample P280-T90 was not possible due to poor-quality CT scans resulting from lower resolution for porosity quantification. Unlike the other samples, this particular CT scan contains sections with grey pixels that were not accurately captured. This issue can be rectified by adjusting the CT scan parameters, including current, voltage, and resolution, for future studies, ensuring more accurate and comprehensive data collection.

2.2. Tensile Mechanical Properties of the Bulk Material. The tensile mechanical properties of the bulk material, manufactured using the same process parameters as the lattice coupons, were obtained from an independent study and are presented in Table 2. A quasistatic tensile test was carried out, with each sample being replicated three times for repeatability. Furthermore, the authors are currently in the process of preparing data from another study that they conducted, utilizing the same builds and large-scale test specimens, for publication. To define the material properties of the FE models, the obtained mechanical properties, such as stiffness, yield stress, and plastic strain, were incorporated into the models based on the bulk material data. This ensures that the FE model accurately represents the mechanical behavior of the lattice structure, taking into account the material characteristics obtained from the bulk material testing. It is worth noting that the FE model is not entirely dependent on this specific data for mechanical properties, as these properties are typical values available in the literature [26, 27].

2.3. Quasistatic Compression Test. The lattice coupons underwent quasistatic compression tests at a 1 mm/min loading speed following the ISO 13314:2011 standard [28] using an Instron 5982 machine. Each sample underwent

Table 1: CT scan measurements of $10 \times 10 \times 10$ lattice structures including cylindrical diameters, strut thickness, node thickness, internal porosity, and R_a [25].

Parameter	As-designed	P280-T30	P280-T60	P280-T90	P210-T30	P360-T30
Cylindrical diameter (μm)	420	396	403	381	348	447
Strut thickness (μm)	420	363	357	344	326	386
Node thickness (μm)	420	447	463	431	399	504
Internal porosity (%)	0	2.17	0.27	—	10.8	0.25
R_a (μm)	0	17	22	21	21	25

Table 2: Mechanical properties of bulk metal obtained from the quasistatic tensile test, including yield stress, stiffness, and UTS [25].

	Tensile P280-T30	Tensile P280-T60	Tensile P280-T90	Tensile P210-T30	Tensile P360-T30
Yield stress (MPa)	1064	1047	1075	1076	1074
Stiffness (GPa)	113	113	112	113	133
UTS (MPa)	1119	1106	1121	1120	1122

three repetitions of the quasistatic compression tests for repeatability. Stiffness, yield stress, and peak stress were considered the indicators of the build quality of the lattice coupons in this study, leading to a focused analysis primarily on these properties over other mechanical characteristics. Therefore, the investigation primarily considered the elastic and plastic behavior of the lattice coupons up to the point of diagonal shear failure, which is characterized by a sudden drop in stress. The effective stress-strain plots (Figure 1) were generated by calculating the effective stress as the ratio of the applied force to the cross-sectional area of the lattice bounding cube and the effective strain as the displacement of the crosshead divided by the original length of the lattice bounding cube [25]. The effective stress-strain plots played a crucial role in determining and summarizing the mechanical properties, as presented in Table 3. The experiment error reported in Table 3 represents the repeatability error observed during the experiments. It was quantified as the maximum value for the ratio of the standard deviation to the mean value of the mechanical properties [25]. These error values offer valuable insights into the consistency and reliability of the compression tests, providing an indication of an acceptable range of error in the experimental results. The numerical error, on the other hand, represents the deviation between the predicted mechanical property values and the experimental values, offering an assessment of the FE model's inaccuracy. The experimental results will be further compared with the numerical results for model validation, which will be comprehensively discussed in Section 4 of this paper. Additionally, the mechanical properties of the as-designed numerical model are provided for comparison with both the experimental results and the numerical results of the as-built lattices.

3. Method

3.1. Modeling and Assumptions.
The FE models were developed using the nonlinear FEM software *MSC Marc*. The CAD models of the quarter section of the diamond lattice coupons were designed using *Autodesk Fusion 360* and then exported to *MSC Marc*, as shown in Figure 2. A solid mesh

was chosen to incorporate the manufacturing defects in the model by adopting a simplified geometry technique, which is not achievable using beam or shell elements. A quadratic 10-node tetrahedron with a mesh size of 0.1 mm was selected to mesh the model. To conduct the virtual compression test on the model, a fixed displacement was applied to the top surface of the lattice structure up to a strain of 0.045 under quasistatic loading conditions. In contrast, the bottom surface of the lattice model was constrained in the loading direction (y-axis), and the symmetric boundary condition was applied to the x and z directions. The bulk tensile properties summarized in Table 2 are used to define the material properties of the model. The stiffness and yield strength were directly input into the model. To define the plasticity, the engineering plastic stress and strain from the tensile tests were converted to true plastic stress and strain using the following equations: $\sigma_{\text{true}} = \sigma_{\text{engineering}} * (1 + \varepsilon_{\text{engineering}})$ and $\varepsilon_{\text{true}} = \ln (1 + \varepsilon_{\text{engineering}})$.

It should be noted that these equations are only valid up to the UTS. Any stress and strain data beyond the UTS was truncated, as the equations cannot accurately represent the material behavior at this point. Certain assumptions constrain the accuracy of the model development process. For instance, Poisson's ratio of the material model was assumed to be 0.34, based on the technical sheet of Ti64ELI [29]. This choice was made to streamline the material characterization process of the bulk material and reduce costs and time. Additionally, a mesh size of 0.1 mm was utilized due to computational constraints of memory deficiency and calculation time, resulting in an approximate 7% loss in accuracy, compared to a convergence mesh of 0.02 mm. To manage computational cost, geometry simplification techniques were implemented. The lattice structure was assumed to be regular and homogeneous. Furthermore, the model focused on investigating the elastic-plastic regions before diagonal shear failure, which is characterized by a sudden drop in stress, specifically around a strain of 0.04-0.05. This range was considered sufficient for obtaining key mechanical properties, such as stiffness, yield stress, and initial peak stress, which were deemed important indicators of the build quality of
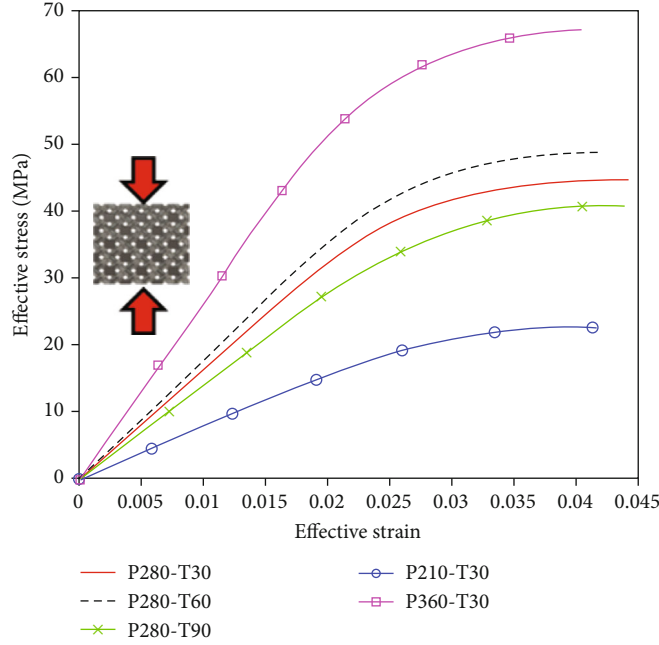
FIGURE 1: Stress-strain plots of lattice coupons exhibiting distinct regions, including the elastic and plastic regions, prior to shear failure [25].

TABLE 3: Mechanical properties of lattices for experimental (Exp) and numerical (Num) results and as-design model for numerical results only as an as-designed model cannot be investigated through experimental methods [25].

	Stiffness (GPa)		Yield stress (MPa)		Peak stress (MPa)		Error (%)	
	Exp	Num	Exp	Num	Exp	Num	Exp	Num
P280-T30	1.6	1.8	39	35	45	46	5	12
P280-T60	1.8	2.0	43	39	52	52	4	10
P280-T90	1.4	1.6	37	32	43	43	4	13
P210-T30	0.7	0.9	20	19	24	25	5	31
P360-T30	2.6	3.0	59	53	70	69	8	17
As-designed	—	2.4	—	44	—	57	—	—

the lattice coupons in this study. As a result, the analysis primarily concentrated on these properties over other mechanical characteristics. All FE models in this study were simulated using high-performance computing clusters (HPCs). The simulations were performed using 16 cores and 16 threads with 360 GB RAM. For computational power and time management, simulations running for more than 72 hours (3 days) are deemed impractical. The proposed models in this study serve as practical solutions, as they require a running time of less than 72 hours. This ensures efficient and manageable simulations for studying the mechanical behavior of lattice structures with manufacturing defects.
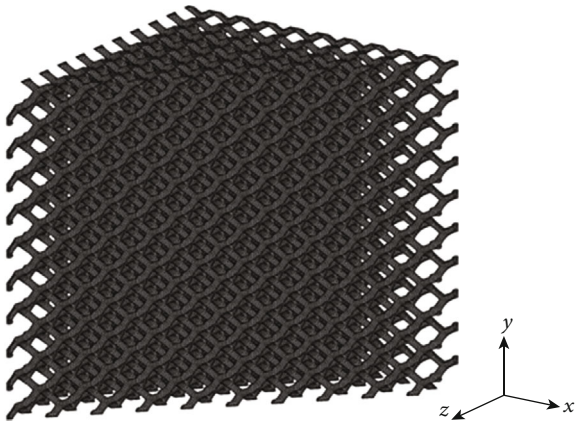
3.2. Geometric Inaccuracy Models

3.2.1. Cylindrical Diameter Model. The cylindrical diameter of the printed lattice coupons, shown in Table 1, deviated from the 420 μm dimension of the as-designed model due to the sensitive nature of the lattice structure to process parameter variation. This discrepancy in dimension introduced geometric inaccuracies between the as-designed model and the actual printed samples, resulting in higher errors in predicting the mechanical properties using FE models. To address this limitation, a cylindrical diameter model was developed. This model maintained the same geometry as the as-designed model but incorporated different dimensions for the cylindrical diameter to match the values obtained from CT scan analysis.

3.2.2. Strut-Node Model. The printed lattice coupons displayed irregular strut geometry with uneven profiles, reflecting inherent manufacturing defects and geometric inaccuracies, unlike the idealized geometry of the numerical

FIGURE 2: Isometric view of the quarter section of the as-designed lattice model with triangular prism shape.
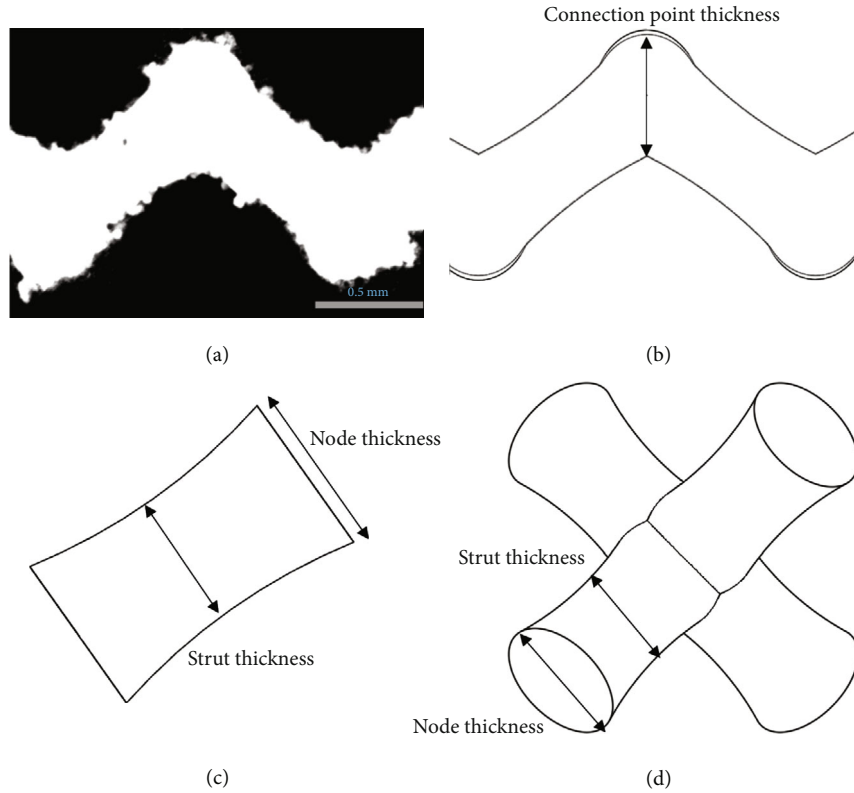
(a)

(b)

(c)

(d)

FIGURE 3: CT scan cross-section image demonstrating a significant difference in thickness values between strut and node regions (a), a diagram of strut-node geometry design (b), node-strut geometry of a single strut with its dimension parameters (c), and node-strut geometry of a unit cell with its dimension parameters (d).

model. As depicted in Figure 3(a), there was a noticeable difference in thickness between the node and strut regions, despite obtaining the cylindrical diameter from the estimated mean of these regions. To better capture this discrepancy, the geometry of the strut in the idealized model was enhanced by modifying it to a lofted cylindrical shape, leading to the creation of the strut-node geometry (Figure 3(b)). This modification involved adjusting the outer edge diameter and middle strut diameter of a single strut as shown in Figure 3(c), based on the node thickness and strut thickness values obtained from Table 1. Subsequently, a unit cell base was constructed using the modified strut dimensions, resulting in the improved strut-node geometry as depicted in Figure 3(d). It is worth noting that the selected node thickness, representing the outer diameter of a single strut, was found to be slightly smaller by 20-30 μm compared to the thickness of the connection points of the struts (Figure 3(b)), which are typically considered as nodes. This variation is attributed to the overlap in strut geometry, leading to the formation of a broader connection region. However, our results, which will be presented in Section 4, demonstrate a good match with experimental results, indicating that this deviation in dimension appears to be acceptable.

3.3. Internal Porosity Model. The impact of internal porosity within the struts of lattice coupons was studied by using the RVE technique with *Digimat* 2021.3 software to homogenize the input material properties of lattice structures. An RVE with dimensions of $0.4 \times 0.4 \times 0.4$ mm was chosen to be close to the greatest strut thickness of 0.386 mm to ensure that the selected pore size in RVEs matches the actual size of pores in the printed sample, as well as maintains a suitable ratio of pore size to strut thickness. The elastoplastic material model was developed based on the results of the bulk tensile test, and internal pores were generated by selecting a generic synthetic microstructure with a void phase (closed pores with a size of 60 μm), as shown in Figure 4. The volume fraction and size of the void were customized in the software to align with the findings from CT scans. For samples with high internal porosity, careful control over the volume fraction and pore size is essential, as discussed further in Section 4. The RVE models were subjected to both uniaxial tensile loading and shear loading to determine the reduced mechanical properties, considering periodic boundary conditions. This evaluation encompassed stiffness, yield stress, and plasticity, taking into account the influence of internal porosity. The obtained mechanical properties were subsequently utilized as input data for the compressive model of the lattice structure.

3.4. Surface Morphology Model. In this study, the impact of rough surface morphology, particularly the presence of extra material attached to the struts, on the lattice structure was also investigated. During CT scan analysis, the inscribed circle method was employed to quantify the cylindrical
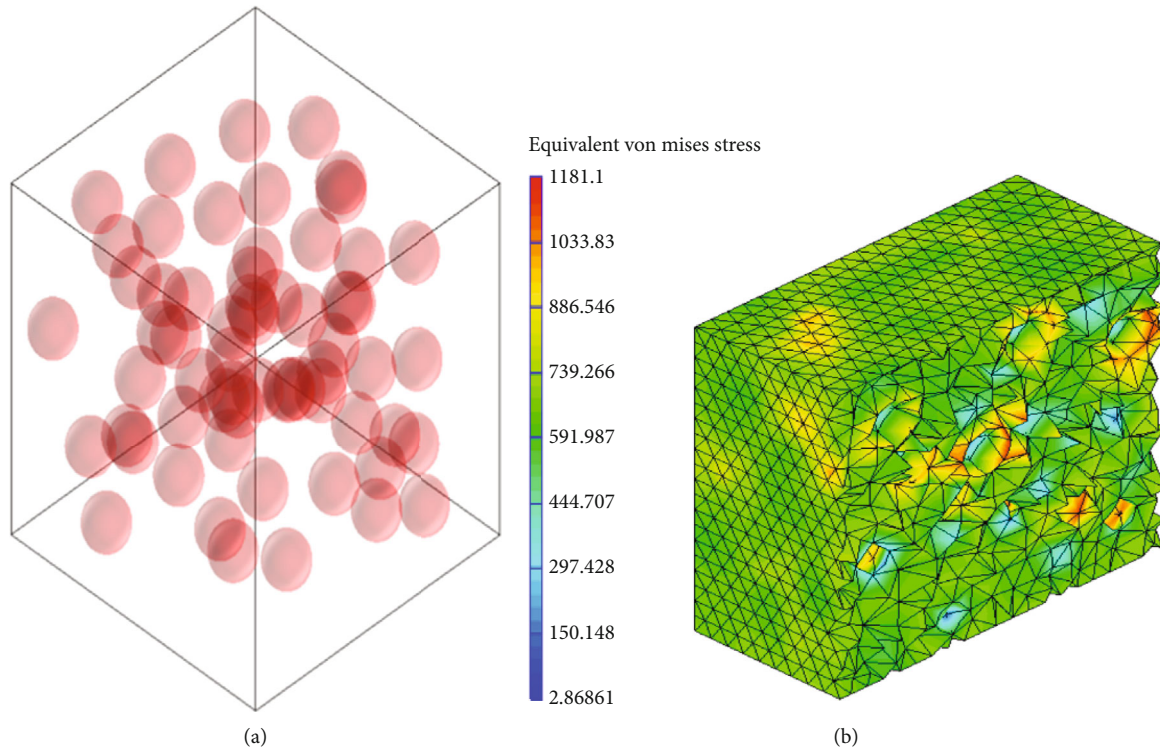
FIGURE 4: RVE with the ideally spherical voids generated using Digimat (a) and cross-section of the simulated RVE model showing equivalent von Mises Stress (b).

diameter, strut thickness, and node thickness, disregarding any extra materials outside of the inscribed circle as depicted in Figure 5(a). However, to account for the influence of these excluded materials and consider surface roughness, a method proposed by Ghosh et al. [22] was implemented. This approach improved the accuracy of representing the surface morphology of the lattice structure. This method utilizes sharp notch-shaped geometric features to represent the surface morphology of the microstrut. Incorporating these features directly into the lattice models was a challenging task in terms of meshing and computational time. To overcome this, the notch-shaped feature was introduced to the single strut rather than the whole lattice structure, as shown in Figure 5(b). The single strut with the notch-shaped feature was subjected to a uniaxial tensile load, and the mechanical properties obtained from this test were used as the material property input of the lattice compressive model. The dimensions of the notch features (Figure 5(c)) were selected to be the same as those used in the work of Ghosh et al. [22]: $0.04\,\mu$m for thickness (t), $50°$ for top angle (α), and $65°$ for bottom angle (β), while the feature-length (r) was selected as a variable parameter to achieve distinct surface roughness levels. To determine the feature-length, R_a values obtained from the CT scan using the numerical code *StrutSurf* developed by Oosterbeek and Jeffers [30] were aligned. Although R_a values were considered in this study as they represent the average deviations from the mean profile, it is worth noting that R_a is only one definition of roughness, and other definitions also exist, such as R_q and R_z. Exploring and investigating other roughness parameters

for surface representation could be beneficial for future research. Determining the most appropriate parameter for surface roughness representation will be a subject of future investigation.

3.5. Final Model. The development of the final model that incorporates all manufacturing defects, i.e., geometry inaccuracies, internal porosity, and surface roughness, involved two main aspects: geometry modeling and input material property definition. In terms of geometry modeling, the initial step was to create an idealized geometry model based on the STL (design) files used for printing. The mean cylindrical diameter of the idealized geometry was then adjusted to match the mean cylindrical value obtained from CT scan analysis (Table 1). To incorporate more accurate CT data, the model was further modified to a strut-node geometry, where the thickness values were obtained from the node regions, and the strut thicknesses were obtained from the CT scan analysis.

For the input material properties defining process, the mechanical properties of the bulk tensile specimen obtained from experimental results were used as input for the porosity-incorporated RVE model. The volume fraction and the size of the void were determined based on the internal porosity value and the average pore diameter obtained from CT scan analysis. The mechanical properties obtained from the RVE were subsequently used as input for the tensile simulation of the microstrut with surface roughness features. In the surface morphology model, the feature-length was selected to align with the R_a values from the CT scans.
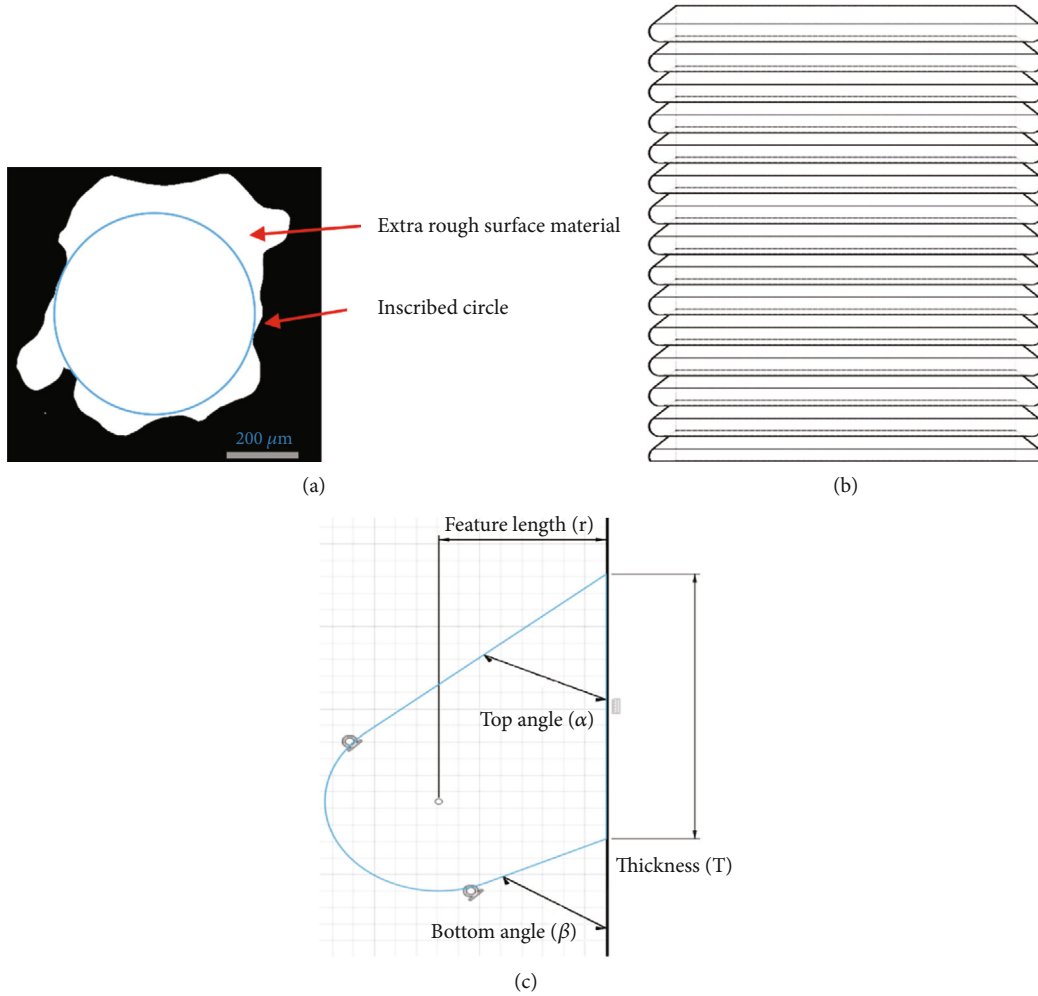
(a)

(b)

(c)

FIGURE 5: A cross-sectional view of a strut with the inscribed circle (a), a single strut with surface roughness features (b), and a diagram of the notch-featured strut with dimensions (c).

Finally, the mechanical properties obtained from the tensile simulation of the microstrut with surface roughness features were used as the material input for the final model with strut-node lofted geometry. It is important to highlight that the final model is not restricted to encompassing all defects; rather, it can also accommodate isolated single manufacturing defects or combinations of two defects. This can be achieved by bypassing specific stages of manufacturing defect design. For example, to incorporate geometrical inaccuracies and internal porosity without considering surface roughness, the surface roughness stage can be omitted.

4. Model Validation

A good agreement between the experimental result and FE numerical result was found for lattice structures as shown in Figure 6. Table 3 compares the mechanical properties obtained from numerical simulation and experiment, along with the maximum numerical error. The maximum numerical error reflects the largest deviation of the numerical results from the experimental result among the mechanical properties. The results show that the final numerical FE model can predict the mechanical properties with a maximum error of 47% observed in P210-T30 for stiffness, 13% observed in P280-T90 for yield stress, and 7% observed in P210-T30 for peak stress. The errors observed in the numerical results can be attributed to two main factors: the selection of the mesh size and the experimental reproducibility error. The mesh size introduced an accuracy error of approximately 7%, compromising the precision of the numerical simulations. Additionally, the experimental reproducibility error, as indicated in Table 3, contributed to the overall discrepancy between the numerical and experimental results. For the four models except P210-T30, the numerical error was found to be less than 17%. The level of error is lower than the 22% error reported in the literature [31]. This numerical error can be partially attributed to a combination of factors, including the cell accuracy error and the experimental reproducibility error. The maximum numerical error observed is only slightly higher than the sum of these two errors, with a difference of approximately 2%. The numerical error of 47% for sample P210-T30 was greater than the sum of those two errors, 12%. Sample P210-T30 exhibited an exceptionally high internal porosity of 11% compared to the other samples.
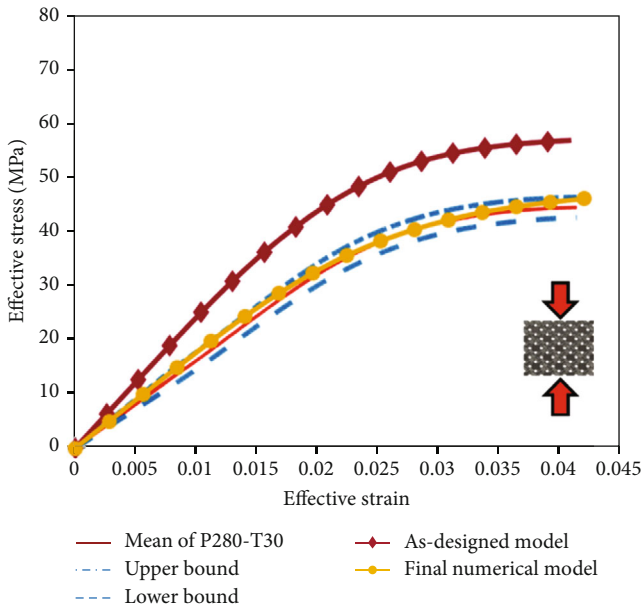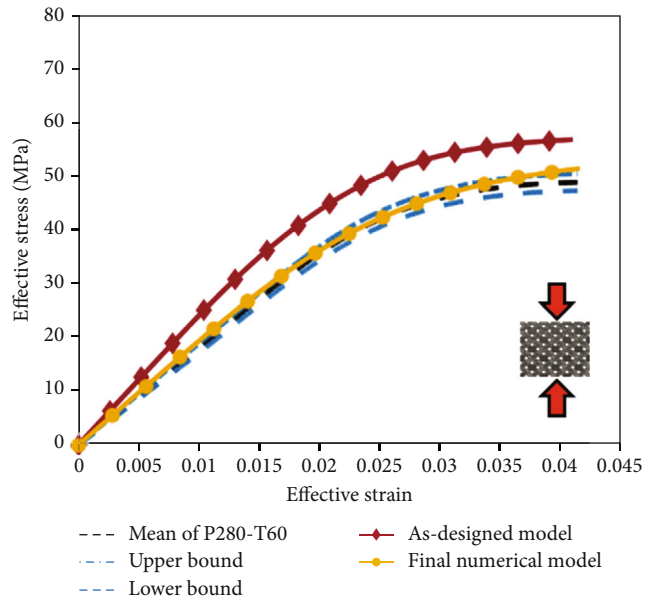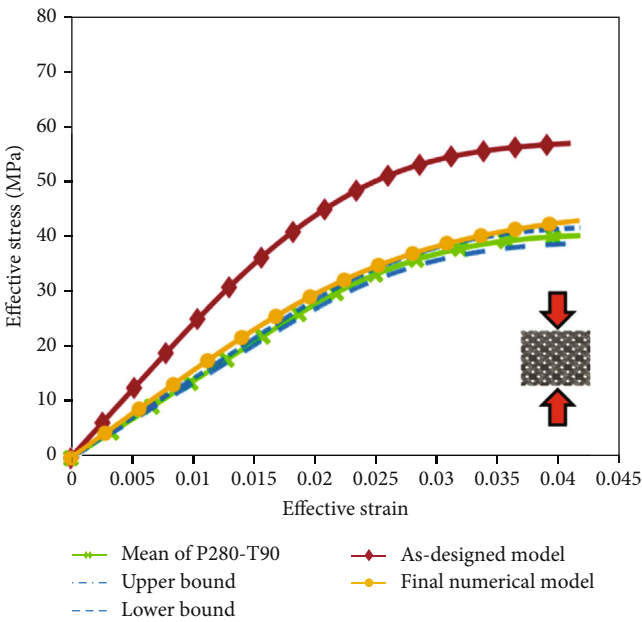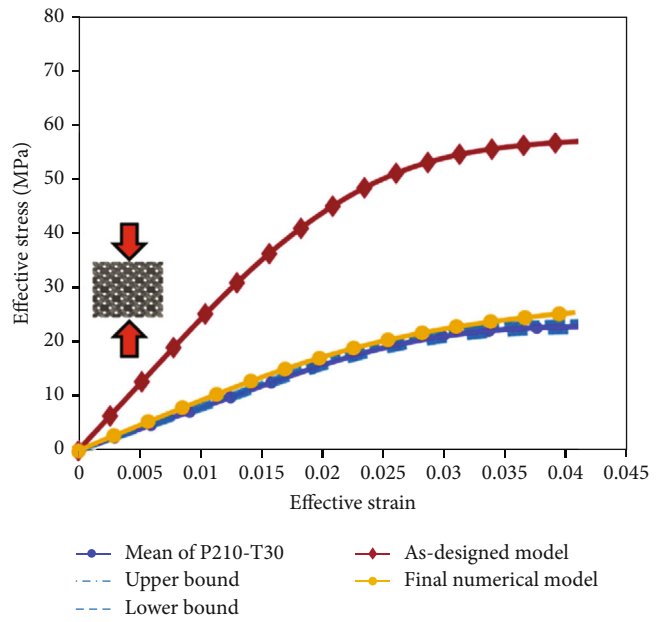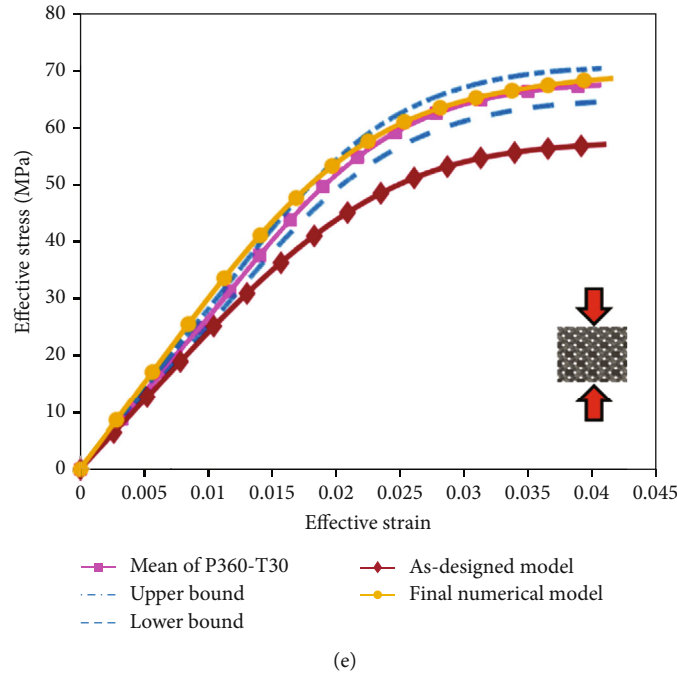
FIGURE 6: Continued.

(e)

FIGURE 6: Stress-strain plots of final models for P280-T30 (a), P280-T60 (b), P280-T90 (c), P210-T30 (d), and P360-T30 (e) compared with the as-designed model and experimental results with upper and lower bounds showing the one standard deviation from the mean.
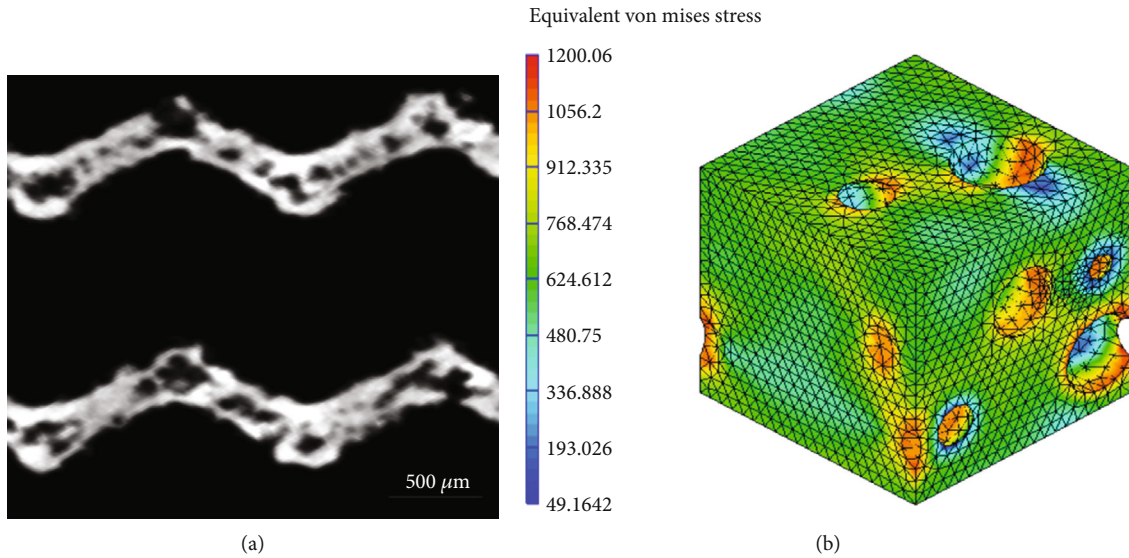

(a)   (b)

FIGURE 7: CT scan image of P210-T30 with interconnected pores and open pores (a) and simulation result of RVE with open pores for P210-T30 (b).

Therefore, special attention was given to developing the RVE for this sample. CT scan analysis shown in Figure 7(a) revealed that sample P210-T30 contained numerous open pores and interconnected closed pores compared to the other samples. To account for this difference, the RVE model for sample P210-T30 incorporated open pores with a pore size of 133 μm (Figure 7(b)), which is significantly greater than the pore size used for the other samples (60 μm), as obtained from the CT scan analysis. The impact of open pores and increased pore size on the mechanical performance of lattice structures was found to be significant. By incorporating these factors into the numerical simulation, a closer agreement between the simulation and experimental results was achieved, reducing the numerical error from 47% to 32%. Although the FE model still overestimated the stiffness by 32%, the absolute deviation was only 0.2 GPa, which is relatively small. Additionally, the numerical error for yield stress and peak stress was found to be less than 7%. To improve the accuracy of predicting the mechanical properties of lattice structures with high porosity, it is crucial to gain a deeper understanding of the types and sizes of pores through future research.

5. Discussion

5.1. Comparison between As-Designed Model and Manufacturing Defect Models. In this section, the effectiveness of each manufacturing defect model will be discussed, following the model development process from the as-designed model to the final model, using stress-strain plots as shown in Figure 8 (models 1-5). For this analysis, we selected sample P280-T30, which exhibits an intermediate severity of manufacturing defects. The as-designed model (model 1) had a cylindrical diameter of $420\,\mu$m, leading to an overestimation of the experimental results. To enhance accuracy, the cylindrical diameter model (model 2) was developed with a diameter of $400\,\mu$m, closely matching the sample P280-T30 (diameter $396\,\mu$m). This improvement resulted in a better match with experimental data, reducing the numerical error in mechanical properties from 49% to 23%. Continuing, the strut-node geometry model (model 3) closely aligned with the experimental results, falling within the upper and lower boundaries. It achieved a further reduction in error to 12% compared to the cylindrical diameter model. The internal porosity model (model 4) was also examined, incorporating both strut-node geometry and porosity. It showed a better match in stiffness with experimental results, reducing the error in stiffness from 10% to 4% compared to the strut-node model. However, it slightly underestimated the plastic stress after the yield point, increasing the error in yield stress from 12% to 18%, and peak stress from 1% to 6%. Additionally, the final roughness model (model 5) was developed, integrating strut-node geometry, porosity, and surface roughness. This final model demonstrated a good match with experimental results, although the plastic stress was higher than that of the porosity model. The numerical error was reduced in the final model from 18% to 12%. The higher mechanical performance of the final model (model 5), in contrast to the internal porosity model (model 4), can be attributed to the notch-strengthening effect [23]. This effect arises from the modeling approach employed for surface roughness [22]. Further elaboration on this topic will be provided in Section 5.2.

Overall, the proposed models effectively incorporated manufacturing defects using CT scans and simplified geometry, resulting in improved matches with experimental results compared to the as-designed model, as presented in Figure 6. Moreover, the adoption of the final model significantly reduced the numerical errors. The numerical errors of the final models, ranging from 10% to 31%, were noticeably less than those of the as-designed model, which ranged from 25% to 247%. By utilizing the final model, the numerical error in stiffness can be reduced up to 216%, yield stress up to 124%, and peak stress up to 134%.

5.2. Impact of Manufacturing Defect Parameters. The influence of manufacturing defects on the mechanical performance of lattice structures was examined through a parametric study involving variations in the cylindrical diameter, internal porosity, and surface roughness. To facilitate these investigations, a cylindrical diameter model with dimensions of $420\,\mu$m, which corresponds to the geometry
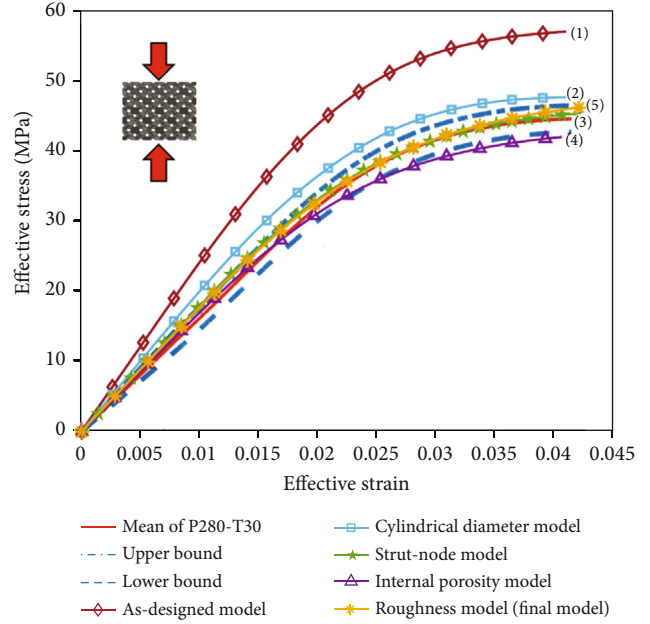

FIGURE 8: The stress-strain plots of different numerical models show the reduction in numerical error with the model developing process (1-5).

of the as-designed lattice models with idealized geometry, was utilized. This model served as the basis for conducting the parametric analyses and assessing the impact of the different parameters on the mechanical properties of the lattice structures.

The Gibson-Ashby model [32] suggested that the relative mechanical properties are influenced by the volume fraction, which is dependent on the cylindrical diameter. In this regard, a parametric study was conducted on the cylindrical diameter to explore its effect on the mechanical performance. The cylindrical diameter of the idealized geometry lattice model was systematically varied between $300\,\mu$m and $500\,\mu$m, with an increment of $20\,\mu$m. The results, shown in Figure 9(a), were utilized to examine the correlations between the relative mechanical properties and the volume fraction using the Gibson-Ashby model equation $X/X\_s = C(\rho/\rho\_s)^\wedge n$. The findings were consistent with the Gibson-Ashby model, as indicated by high R^2 values of 1, 0.9986, and 0.9994 for relative stiffness, yield strength, and peak strength, respectively. These results suggest a positive power correlation between the cylindrical diameter and mechanical properties.

To quantify the detrimental effect of internal porosity on mechanical properties, the porosity varied from 0.2 to 15%. This range was chosen to cover a minimum number of pores (1) for a void fraction of 0.2% while ensuring that porosity exceeding 15% was avoided, as they are impractical in terms of manufacturability. The parametric study on internal porosity demonstrated a clear correlation between the percentage of internal porosity and the mechanical performance of both the RVE and the lattice structure. As shown in Figure 9(b), the mechanical properties showed a linear decrease with increasing internal porosity. The presence of
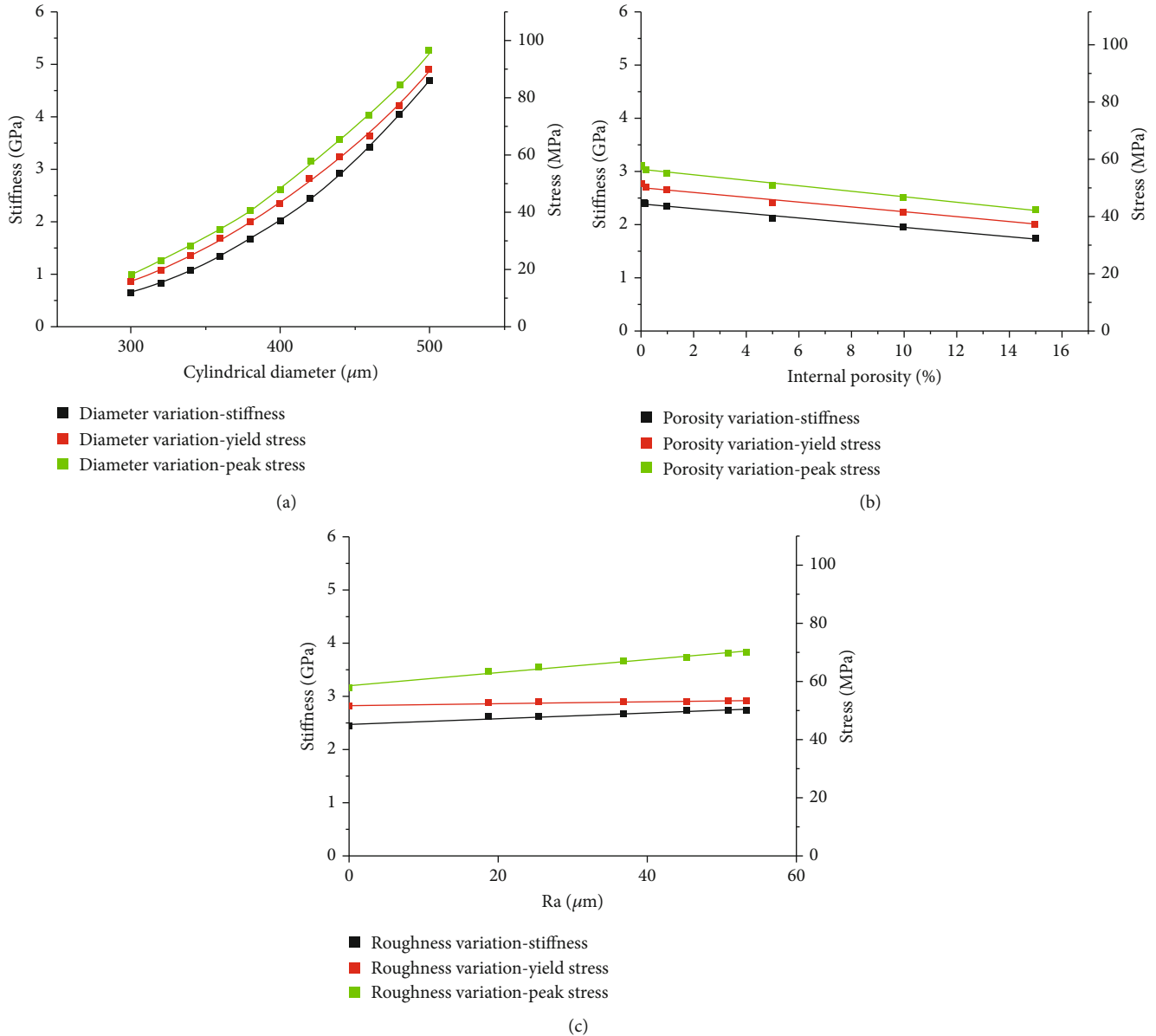
(a)

(b)

(c)

FIGURE 9: The trends of mechanical properties (stiffness, yield stress, and peak stress) with variations in cylindrical diameter (a), internal porosity (b), and R_a (c).

internal pores reduced the amount of material present in the given volume of RVE by providing a vacant space and acting as stress raisers as shown in Figure 4(b), negatively affecting the mechanical properties of RVE and thereby lattice structures.

The parametric study on surface roughness involved varying the feature-length from 0 to 0.1 μm with increments of 0.02 μm, including 0.01 μm. This range was selected to encompass the minimum and maximum achievable sizes for the feature geometry, ensuring that any feature-length outside of this range would significantly alter the intended design. The corresponding R_a values for these feature-lengths are 0, 19, 26, 32, 37, 46, 51, and 54 μm. The results of the tensile simulation were consistent with those reported by Ghosh et al. [22]. The mechanical performance of the

microstrut increased as the feature-length (r) increased, primarily due to the notch-strengthening effect caused by the presence of surface notches [23]. Compared to the model without surface roughness ($r = 0 \mu$m), the model with a feature-length of 0.01 μm (R_a of 19 μm) exhibited approximately 26% higher plastic stress and 11% higher stiffness. This indicated that the presence of the surface roughness feature had a more significant impact on increasing the plastic stress of the microstrut compared to its effect on stiffness. Similar trends were observed in other lattice models with increasing feature-lengths. Furthermore, the yield stress and peak stress of the lattice model showed a linear increase at a gentle pace with increasing feature-length as depicted in Figure 9(c), while the increase in stiffness was relatively weaker. This observation suggested that the additional
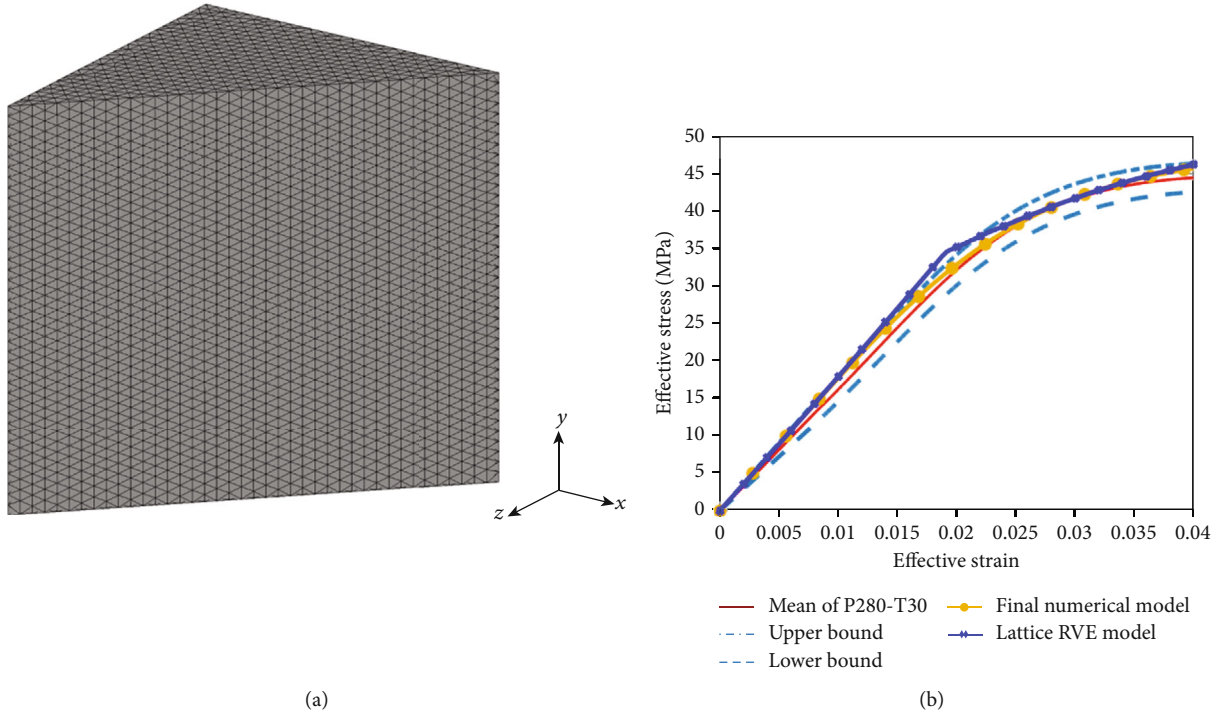
(a)

(b)

FIGURE 10: The isometric view of the solid-infilled model which replaces the lattice structure through lattice RVE modeling (a) and stress-strain plots of the lattice RVE model compared with experimental and numerical results (b).

material on the surface of the strut, acting as surface roughness, did not significantly affect the stiffness but played a more prominent role in increasing the plastic stress of the microstrut.

The study examined the impact of manufacturing defects and found varying degrees of sensitivity in mechanical performance. The sensitivities of mechanical performance to manufacturing defect parameters were compared intuitively by referring to plots (Figure 9). The mechanical properties of the lattice model increased with increasing cylindrical diameter, following a power function, while linear trends in mechanical properties were observed for increasing internal porosity and R_a. Internal porosity exhibited a negative linear trend with a steeper slope compared to R_a values, which had a positive linear trend with a gentle slope. The parameter sensitivity study demonstrated that the mechanical performance of the FE model was highly sensitive to the cylindrical diameter, followed by the internal porosity, whereas the impact of R_a was relatively weak compared to the other two parameters. This finding highlights the importance of controlling the cylindrical diameter and internal porosity through process parameter optimization to enhance the mechanical performance of the lattice structure as well as build quality.

5.3. Manufacturing Defect-Incorporated RVE for Replacing Lattice Parts. In this section, a practical application of our proposed final model will be suggested. The user can utilize the final model as RVE for homogenization, as a final model with a normalized size of 10 is sufficient to represent the homogenized lattice structure according to the literature [33]. The stress-strain plots and mechanical properties

obtained from the final model can be used as material input for numerical simulations of parts containing lattice structures, with the lattice structure being replaced by a solid-infilled model.

To validate this approach, an example is shown in which the lattice structure in Figure 2 is replaced by a solid-infilled prism, as depicted in Figure 10(a). The final lattice model is used as an RVE, and the stress-strain plots from the final model of sample P280-T30 (Figure 6(a)) are employed as material input for the solid prism. The simulation is conducted under the same conditions as the lattice model. The results presented in Figure 10(b) demonstrate a good agreement between the numerical results and lattice RVE models with the solid prism. Unlike the experimental and numerical results, the lattice RVE model shows a clear yield point, which is the transition point from the elastic to the plastic region. The mechanical properties of the final numerical model and the lattice RVE model were found to be almost identical, with an error of less than 1%. However, the yield strain in the final numerical model was found to be 0.0027 smaller. This discrepancy is due to the use of the 0.002 offset method on the final numerical model to find the yield stress, which is not clearly observed from the stress-strain plot. In contrast, the offset method was not used in the lattice RVE model, as it has a clear yield point.

This approach not only simplifies the numerical simulation of parts containing lattice structures, leading to a reduction in computational cost and time, but also provides the user with the flexibility to perform parametric studies on manufacturing defects using RVE. This enables a deeper understanding of how these defects impact the performance of the application. Moreover, our model allows the user to

easily tailor and control the level of geometrical inaccuracies, internal porosity, and surface roughness. This level of control is invaluable for optimizing the mechanical properties of lattice structures to meet specific engineering requirements. By utilizing our proposed model, engineers and researchers can confidently explore the effects of various manufacturing defects on the lattice structures and fine-tune their designs to achieve the desired mechanical performance. This enables more efficient and accurate development of lattice structures for a wide range of applications, ultimately leading to enhanced performance and reliability in real-world scenarios.

6. Conclusion

This study introduces a novel numerical approach to predict the elastic-plastic behavior of lattice structures fabricated using L-PBF with diamond unit cells. The proposed model incorporates various manufacturing defects, including geometric inaccuracies, internal porosity, and surface roughness, utilizing CT scan data to accurately characterize the lattice structures. By adjusting input material properties and geometry, the final numerical FE model demonstrates the capability to predict the mechanical properties of the lattice structures with good accuracy. The maximum errors observed for stiffness, yield stress, and peak stress are 17%, 13%, and 7%, respectively, except for sample P210-T30, which exhibited notably high internal porosity. The parameter sensitivity study demonstrated that the mechanical performance of the FE model was highly sensitive to the cylindrical diameter, followed by the internal porosity, whereas the impact of R_a was relatively weak compared to the other two parameters.

The proposed model offers an efficient and valuable approach for conducting complex numerical simulations of lattice structures with manufacturing defects, for the first time incorporating geometrical error, porosity, and surface roughness in one model. It represents a promising tool for developing RVEs that incorporate manufacturing defects. By replacing intricate lattice structures with solid-infilled features in simulations, significant reductions in computational cost and time can be achieved, making it a practical and accessible solution for industry users. This numerical approach opens up new possibilities for studying the impact of manufacturing defects on lattice structures, allowing engineers and researchers to optimize the mechanical properties of lattice designs for specific applications. With the ability to accurately simulate and understand the behavior of lattice structures with defects, the proposed model can lead to improved and more reliable lattice-based components in various engineering fields.

While the current numerical model is straightforward to implement, yields dependable results, and is easily interrogated, it has limitations. In its current state, the model lacks the capability to explore correlations between different defect types, as it assesses the mechanical impact of each defect type individually at a specific scale. Additionally, it does not consider the stochastic nature of defects, such as variations in size and position within the specimen. These aspects could be addressed in potential future developments.

References

[1] M. Benedetti, A. du Plessis, R. O. Ritchie, M. Dallago, S. M. J. Razavi, and F. Berto, "Architected cellular materials: a review on their mechanical properties towards fatigue-tolerant design and fabrication," *Materials Science and Engineering R: Reports*, vol. 144, article 100606, 2021.

[2] A. du Plessis, S. M. J. Razavi, M. Benedetti et al., "Properties and applications of additively manufactured metallic cellular materials: a review," *Progress in Materials Science*, vol. 125, article 100918, 2022.

[3] M. McGregor, S. Patel, S. McLachlin, and M. Vlasea, "Architectural bone parameters and the relationship to titanium lattice design for powder bed fusion additive manufacturing," *Additive Manufacturing*, vol. 47, article 102273, 2021.

[4] B. Blakey-Milner, P. Gradl, G. Snedden et al., "Metal additive manufacturing in aerospace: a review," *Materials & Design*, vol. 209, article 110008, 2021.

[5] T. DebRoy, T. Mukherjee, J. O. Milewski et al., "Scientific, technological and economic issues in metal printing and their solutions," *Nature Materials*, vol. 18, no. 10, pp. 1026–1032, 2019.

[6] S. Murchio, M. Dallago, F. Zanini et al., "Additively manufactured Ti-6Al-4V thin struts via laser powder bed fusion: Effect of building orientation on geometrical accuracy and mechanical properties," *Journal of the Mechanical Behavior of Biomedical Materials*, vol. 119, article 104495, 2021.

[7] N. R. Mathe, L. C. Tshabalala, S. Hoosain, L. Motibane, and A. du Plessis, "The effect of porosity on the mechanical properties of Ti-6Al-4V components manufactured by high-power selective laser melting," *International Journal of*

Advanced Manufacturing Technology, vol. 115, no. 11-12, pp. 3589–3597, 2021.

[8] M. Güden, A. T. Alpkaya, B. A. Hamat et al., "The quasi-static crush response of electron-beam-melt Ti6Al4V body-centred-cubic lattices: the effect of the number of cells, strut diameter and face sheet," *Strain*, vol. 58, no. 3, 2022.

[9] B. Barnes, B. B. Babamiri, G. Demeneghi, A. Soltani-Tehrani, N. Shamsaei, and K. Hazeli, "Quasi-static and dynamic behavior of additively manufactured lattice structures with hybrid topologies," *Additive Manufacturing*, vol. 48, article 102466, 2021.

[10] Z. A. Qureshi, S. A. B. Al-Omari, E. Elnajjar, O. Al-Ketan, and R. A. Al-Rub, "On the effect of porosity and functional grading of 3D printable triply periodic minimal surface (TPMS) based architected lattices embedded with a phase change material," *International Journal of Heat and Mass Transfer*, vol. 183, article 122111, 2022.

[11] O. Weeger, I. Valizadeh, Y. Mistry, and D. Bhate, "Inelastic finite deformation beam modeling, simulation, and validation of additively manufactured lattice structures," *Additive Manufacturing Letters*, vol. 4, article 100111, 2023.

[12] S. Van Bael, G. Kerckhofs, M. Moesen, G. Pyka, J. Schrooten, and J. P. Kruth, "Micro-CT-based improvement of geometrical and mechanical controllability of selective laser melted Ti6Al4V porous structures," *Materials Science and Engineering A*, vol. 528, no. 24, pp. 7423–7431, 2011.

[13] G. Kasperovich, J. Haubrich, J. Gussone, and G. Requena, "Correlation between porosity and processing parameters in TiAl6V4 produced by selective laser melting," *Materials and Design*, vol. 105, pp. 160–170, 2016.

[14] J. C. Fox, S. P. Moylan, and B. M. Lane, "Effect of process parameters on the surface roughness of overhanging structures in laser powder bed fusion additive manufacturing," in *Procedia CIRP*, pp. 131–134, Elsevier B.V., 2016.

[15] F. Zanini, M. Sorgato, E. Savio, and S. Carmignato, "Dimensional verification of metal additively manufactured lattice structures by X-ray computed tomography: use of a newly developed calibrated artefact to achieve metrological traceability," *Additive Manufacturing*, vol. 47, article 102229, 2021.

[16] A. Du Plessis, I. Yadroitsev, I. Yadroitsava, and S. G. Le Roux, "X-Ray microcomputed tomography in additive manufacturing: a review of the current technology and Applications," *Additive Manufacturing*, vol. 5, no. 3, pp. 227–247, 2018.

[17] L. M. Evans, E. Sözümert, B. E. Keenan, C. E. Wood, and A. du Plessis, "A review of image-based simulation applications in high-value manufacturing," *Archives of Computational Methods in Engineering*, vol. 30, no. 3, pp. 1495–1552, 2023.

[18] S. I. Park, D. W. Rosen, S. Kyum Choi, and C. E. Duty, "Effective mechanical properties of lattice material fabricated by material extrusion additive manufacturing," *Additive Manufacturing*, vol. 1-4, pp. 12–23, 2014.

[19] M. Montemurro, G. Bertolino, and T. Roiné, "A general multiscale topology optimisation method for lightweight lattice structures obtained through additive manufacturing technology," *Composite Structures*, vol. 258, article 113360, 2021.

[20] X. Cao, Y. Jiang, T. Zhao et al., "Compression experiment and numerical evaluation on mechanical responses of the lattice structures with stochastic geometric defects originated from additive- manufacturing," *Composites Part B: Engineering*, vol. 194, article 108030, 2020.

[21] B. Lozanovski, M. Leary, P. Tran et al., "Computational modelling of strut defects in SLM manufactured lattice structures," *Materials & Design*, vol. 171, article 107671, 2019.

[22] A. Ghosh, A. Kumar, X. Wang, A. M. Kietzig, and M. Brochu, "Analysis of the effect of surface morphology on tensile behavior of LPBF SS316L microstruts," *Materials Science and Engineering A*, vol. 831, article 142226, 2022.

[23] X. Lei, C. Li, X. Shi, X. Xu, and Y. Wei, "Notch strengthening or weakening governed by transition of shear failure to normal mode fracture," *Scientific Reports*, vol. 5, no. 1, 2015.

[24] A. du Plessis, S. G. le Roux, and A. Guelpa, "The CT Scanner Facility at Stellenbosch University: an open access X-ray computed tomography laboratory," *Nuclear Instruments and Methods in Physics Research*, vol. 384, pp. 42–49, 2016.

[25] M. Park, M. P. Venter, and A. du Plessis, "Using a lattice structure for build quality monitoring tool in metal additive manufacturing," Unpublished results.

[26] H. Ali, H. Ghadbeigi, and K. Mumtaz, "Processing parameter effects on residual stress and mechanical properties of selective laser melted Ti6Al4V," *Journal of Materials Engineering and Performance*, vol. 27, no. 8, pp. 4059–4068, 2018.

[27] H. Gong, K. Rafi, H. Gu, G. D. Janaki Ram, T. Starr, and B. Stucker, "Influence of defects on mechanical properties of Ti-6Al-4V components produced by selective laser melting and electron beam melting," *Materials and Design*, vol. 86, pp. 545–554, 2015.

[28] ISO Standard, ISO 13314, *Mechanical Testing of Metals – Ductility Testing – Compression Test for Porous and Cellular Metals*, International Organization of Standards, Switzerland, 2011, http://www.iso.org/.

[29] EOS, EOS Titanium Ti64ELIhttps://www.eos.info/03_system-related-assets/material-related-contents/metal-materials-and-examples/metal-material-datasheet/titan/ti64/eos_ti64eli_9011-0017_9011-0040_m290_mds_06-22_en.pdf, 2022.

[30] R. N. Oosterbeek and J. R. T. Jeffers, "StrutSurf: a tool for analysis of strut morphology and surface roughness in additively manufactured lattices," *SoftwareX*, vol. 18, article 101043, 2022.

[31] J. Kadkhodapour, H. Montazerian, A. C. Darabi et al., "Failure mechanisms of additively manufactured porous biomaterials: effects of porosity and type of unit cell," *Journal of the Mechanical Behavior of Biomedical Materials*, vol. 50, pp. 180–191, 2015.

[32] L. Gibson and M. Ashby, *Cellular solids*, Cambridge University Press, 1997.

[33] E. W. Andrews, G. Gioux, P. Onck, and L. J. Gibson, "Size effects in ductile cellular solids. Part II: experimental results," *International Journal of Mechanical Sciences*, vol. 43, pp. 701–713, 2001.